INTERNATIONAL JOURNAL FOR NUMERICAL METHODS IN FLUIDS, VOL. 11, 697–717 (1990)

FINITE ELEMENT ANALYSIS OF CONFINED TURBULENT SWIRLING FLOWS

A. C. BENIM*

Institut für Verfahrenstechnik und Dampfkesselwesen, Universität Stuttgart, Pfaffenwaldring 23, D-7000 Stuttgart 80, F.R.G.

SUMMARY

The finite element method is applied to incompressible and statistically steady confined turbulent swirling flows. A velocity–pressure formulation is employed. The momentum and continuity equations are solved using a segregated algorithm. Two turbulence models, namely the standard k–ε model and the algebraic stress model, are considered. It is shown that the algebraic stress model leads to significantly more accurate results in swirling flows compared to the k–ε model. A novel way of implementing the algebraic stress model is presented in which the stresses are coupled to the Navier–Stokes equations in such a way that they 'correct' the effective viscosity hypothesis. This formulation seems to provide a convenient approach for finite elements. In deriving the discretization equations, a streamline-upwind/Petrov–Galerkin method is employed. Comparisons performed between various upwind schemes show that the numerical solution may be substantially affected by the particular upwind procedure used. The analysis is extended to the prediction of particle motion in turbulent swirling flow fields. Here the fluid turbulence is modelled adopting a stochastic approach. The influence of turbulence modelling on particle movement is investigated.

KEY WORDS Finite elements Turbulent swirling flows Algebraic stress model Particle motion

INTRODUCTION

Turbulent swirling flows are encountered in many important engineering applications.[1] We are particularly interested in flows in combustors and furnaces.[2,3] Here a swirl component is often imparted to the axial flow in order to achieve a stably burning flame or to influence the flame shape. Using standard finite difference codes,[4] some difficulties are encountered in the simulation of such flows. First, geometrical details of swirl burners cannot always easily be captured by a finite difference grid. Secondly, the extreme skewness of the flow direction to the orthogonal grid lines may produce excessive amounts of false diffusion using upwind or hybrid differencing. The finite element method, on the other hand, can handle completely unstructured grids. Thus solution domains of any shape can be conveniently discretized and particular features of the flow can effectively be resolved by local refinements. Further, the streamline-upwind procedures of finite elements[5,6] seem to provide convenient means of reducing the false diffusion. Therefore we expect some benefits from the application of the finite element method to turbulent swirling flows. This is the scope of the present investigation.

In the present study the attention is focused on incompressible and statistically steady turbulent swirling flows. A primitive-variables formulation is preferred in the analysis. For the solution of the momentum and continuity equations, a segregated formulation is employed,[7] where a

* Present address: ABB Turbo Systems Ltd., Thermal Machinery Lab., CH-5401 Baden, Switzerland.

0271–2091/90/140697–21$10.50
© 1990 by John Wiley & Sons, Ltd.
Received 12 June 1989

discretization equation for pressure corrections is obtained directly from the discretized continuity equation, considering the velocity–pressure relationships established in the discretized momentum equations.

Two-equation turbulence models[8] based on a turbulent viscosity hypothesis (especially the k–ε model[8]) are being almost exclusively employed by finite difference[4] and finite element[9-11] codes. Although these models predict many kinds of flows successfully, their performance in flows with streamline curvature and rotation is often found to be insufficient.[12-14] It is generally argued that curvature and rotation effects produce a highly non-isotropic turbulence structure, which cannot adequately be described by two-equation turbulence models based on a turbulent viscosity hypothesis. Some authors have sought to improve the k–ε model by modifying the source term of the dissipation equation or the turbulent viscosity constant.[12-14] Nevertheless, such modifications often suffer from not possessing enough universality. In general, without considering the curvature and rotation effects on the individual turbulent stresses, a major improvement in turbulence modelling shall not be expected, an issue calling for higher-order turbulence closures.

In the present study the algebraic stress model[15] is employed, which provides a principally more accurate turbulence model compared to the k–ε model, without an excessive increase in computational effort. To the best of the author's knowledge, this paper demonstrates the first application of the full algebraic stress model in finite elements. This restricted use of the algebraic stress model is, in our opinion, partly due to the problems associated with the coupling of the turbulent stresses into the Navier–Stokes equations. In the present paper we propose a simple and, especially for finite element formulations, convenient way of implementing the algebraic stress model in which the stresses obtained from the algebraic stress equations are coupled with the Navier–Stokes equations in such a way that they 'correct' the effective viscosity hypothesis.

Discretization equations are upwinded by a 'discontinuity-capturing' version of the streamline-upwind/Petrov–Galerkin method.[6] In order to see the effect of different levels of false diffusion on the numerical solution, computations are also performed using alternative upwind facilities and results are compared.

The investigation is extended to the prediction of particle motion in a turbulent swirling flow field. The influence of fluid turbulence on particle motion is modelled adopting a stochastic approach. Results are compared for alternative turbulence models.

GOVERNING EQUATIONS

For incompressible, statistically steady and axisymmetrical turbulent flows the Reynolds-averaged[8] momentum and continuity equations can be expressed as

$$\rho\left(\bar{u}\frac{\partial\bar{u}}{\partial x}+\bar{v}\frac{\partial\bar{u}}{\partial r}\right)=-\frac{\partial\bar{p}}{\partial x}+\frac{\partial}{\partial x}\left(2\mu\frac{\partial\bar{u}}{\partial x}\right)+\frac{1}{r}\frac{\partial}{\partial r}\left[r\mu\left(\frac{\partial\bar{u}}{\partial r}+\frac{\partial\bar{v}}{\partial x}\right)\right]+\frac{\partial}{\partial x}(-\rho\overline{u'^2})+\frac{1}{r}\frac{\partial}{\partial r}(-r\rho\overline{u'v'}), \tag{1}$$

$$\rho\left(\bar{u}\frac{\partial\bar{v}}{\partial x}+\bar{v}\frac{\partial\bar{v}}{\partial r}-\frac{\bar{w}^2}{r}\right)=-\frac{\partial\bar{p}}{\partial r}+\frac{\partial}{\partial x}\left[\mu\left(\frac{\partial\bar{u}}{\partial r}+\frac{\partial\bar{v}}{\partial x}\right)\right]+\frac{1}{r}\frac{\partial}{\partial r}\left(2r\mu\frac{\partial\bar{v}}{\partial r}\right)-2\mu\frac{\bar{v}}{r^2}+\frac{\partial}{\partial x}(-\rho\overline{u'v'})+\frac{1}{r}\frac{\partial}{\partial r}(-r\rho\overline{v'^2})-\frac{1}{r}(-\rho\overline{w'^2}), \tag{2}$$

$$\rho\left(\bar{u}\frac{\partial\bar{w}}{\partial x}+\bar{v}\frac{\partial\bar{w}}{\partial r}+\frac{\bar{v}\bar{w}}{r}\right)=\frac{\partial}{\partial x}\left(\mu\frac{\partial\bar{w}}{\partial x}\right)+\frac{1}{r}\frac{\partial}{\partial r}\left(r\mu\frac{\partial\bar{w}}{\partial r}\right)-\frac{\partial}{\partial r}(r\mu)\frac{\bar{w}}{r^2}$$

$$+\frac{\partial}{\partial x}(-\rho\overline{u'w'})+\frac{1}{r}\frac{\partial}{\partial r}(-r\rho\overline{v'w'})+\frac{1}{r}(-\rho\overline{v'w'}), \tag{3}$$

$$\frac{\partial\bar{u}}{\partial x}+\frac{\bar{v}}{r}+\frac{\partial\bar{v}}{\partial r}=0. \tag{4}$$

The pair correlations in equations (1)–(3), i.e. the terms $-\rho\overline{u'^2}$, $-\rho\overline{v'^2}$, $-\rho\overline{w'^2}$, $-\rho\overline{u'v'}$, $-\rho\overline{u'w'}$ and $-\rho\overline{v'w'}$, are the so-called Reynolds stresses, which must be specified by a convenient turbulence model.

The k–ε model

The k–ε turbulence model[8] is based on a turbulent viscosity hypothesis. Here the Reynolds stresses are modelled in analogy to the viscous stresses by the following relations:

$$\begin{aligned}
-\rho\overline{u'^2}&=2\mu_t\frac{\partial\bar{u}}{\partial x}-\tfrac{2}{3}\rho\bar{k}, & -\rho\overline{u'v'}&=\mu_t\left(\frac{\partial\bar{u}}{\partial r}+\frac{\partial\bar{v}}{\partial x}\right),\\
-\rho\overline{v'^2}&=2\mu_t\frac{\partial\bar{v}}{\partial r}-\tfrac{2}{3}\rho\bar{k}, & -\rho\overline{u'w'}&=\mu_t\frac{\partial\bar{w}}{\partial x},\\
-\rho\overline{w'^2}&=2\mu_t\frac{\bar{v}}{r}-\tfrac{2}{3}\rho\bar{k}, & -\rho\overline{v'w'}&=\mu_t\left(\frac{\partial\bar{w}}{\partial r}-\frac{\bar{w}}{r}\right).
\end{aligned} \tag{5}$$

In the k–ε model the turbulent viscosity in (5) is given by

$$\mu_t=\rho C_D\bar{k}^2/\bar{\varepsilon}. \tag{6}$$

For high Reynolds numbers the transport equations of k and ε can be expressed in the general form[8]

$$\rho\left(\bar{u}\frac{\partial\bar{\phi}}{\partial x}+\bar{v}\frac{\partial\bar{\phi}}{\partial r}\right)-D_\phi=S_\phi. \tag{7}$$

The term D_ϕ in (7) denotes the diffusive transport. In the standard k–ε model this term is given by

$$D_\phi=\frac{\partial}{\partial x}\left[\left(\frac{\mu_t+\mu}{\sigma_{\phi,e}}\right)\frac{\partial\bar{\phi}}{\partial x}\right]+\frac{1}{r}\frac{\partial}{\partial r}\left[r\left(\frac{\mu_t+\mu}{\sigma_{\phi,e}}\right)\frac{\partial\bar{\phi}}{\partial r}\right]. \tag{8}$$

The source terms for k and ε in (7) are given by

$$S_k=\rho(P-\varepsilon), \tag{9}$$

$$S_\varepsilon=C_1\rho P\bar{\varepsilon}/\bar{k}-C_2\rho\bar{\varepsilon}^2/\bar{k}. \tag{10}$$

In equations (9) and (10) the term P represents the production of k and is defined by

$$P=-\left[\overline{u'^2}\left(\frac{\partial\bar{u}}{\partial x}\right)+\overline{v'^2}\left(\frac{\partial\bar{v}}{\partial r}\right)+\overline{w'^2}\left(\frac{\bar{v}}{r}\right)+\overline{u'v'}\left(\frac{\partial\bar{u}}{\partial r}+\frac{\partial\bar{v}}{\partial x}\right)+\overline{u'w'}\left(\frac{\partial\bar{w}}{\partial x}\right)+\overline{v'w'}\left(\frac{\partial\bar{w}}{\partial r}-\frac{\bar{w}}{r}\right)\right]. \tag{11}$$

Substitution of (5) into (11) gives an expression for P in terms of turbulent viscosity, mean velocity gradients and turbulence kinetic energy.

The algebraic stress model

In the algebraic stress model, proposed by Rodi,[15] the local values of Reynolds stresses are not assumed to be proportional to the mean velocity gradients (5), but are obtained directly by solving

algebraic equations which are derived from Reynolds stress transport equations under certain assumptions.[15] For cylindrical–polar co-ordinates these algebraic Reynolds stress equations[15] can be expressed in matrix form as follows:

$$\begin{bmatrix} \alpha+2\dfrac{\partial\bar{u}}{\partial x} & -\dfrac{\partial\bar{v}}{\partial r} & -\dfrac{\bar{v}}{r} & -\left(\dfrac{\partial\bar{v}}{\partial x}-2\dfrac{\partial\bar{u}}{\partial r}\right) & -\dfrac{\partial\bar{w}}{\partial x} & -\left(\dfrac{\partial\bar{w}}{\partial r}-\dfrac{\bar{w}}{r}\right) \\ -\dfrac{\partial\bar{u}}{\partial x} & \alpha+2\dfrac{\partial\bar{v}}{\partial r} & -\dfrac{\bar{v}}{r} & -\left(\dfrac{\partial\bar{u}}{\partial r}-2\dfrac{\partial\bar{v}}{\partial x}\right) & -\dfrac{\partial\bar{w}}{\partial x} & -\left(\dfrac{\partial\bar{w}}{\partial r}+2\dfrac{\bar{w}}{r}\right) \\ -\dfrac{\partial\bar{u}}{\partial x} & -\dfrac{\partial\bar{v}}{\partial r} & \alpha+2\dfrac{\bar{v}}{r} & -\left(\dfrac{\partial\bar{u}}{\partial r}+\dfrac{\partial\bar{v}}{\partial x}\right) & 2\dfrac{\partial\bar{w}}{\partial x} & 2\dfrac{\partial\bar{w}}{\partial r}+\dfrac{\bar{w}}{r} \\ \dfrac{\partial\bar{v}}{\partial x} & \dfrac{\partial\bar{u}}{\partial r} & 0 & \beta-\dfrac{\bar{v}}{r} & -\dfrac{\bar{w}}{r} & 0 \\ \dfrac{\partial\bar{w}}{\partial x} & 0 & 0 & \dfrac{\partial\bar{w}}{\partial r} & \beta-\dfrac{\partial\bar{v}}{\partial r} & \dfrac{\partial\bar{u}}{\partial r} \\ 0 & \dfrac{\partial\bar{w}}{\partial r} & -\dfrac{\bar{w}}{r} & \dfrac{\partial\bar{w}}{\partial x} & \dfrac{\partial\bar{v}}{\partial x} & \beta-\dfrac{\partial\bar{u}}{\partial x} \end{bmatrix} \begin{bmatrix} \rho\overline{u'^2} \\ \rho\overline{v'^2} \\ \rho\overline{w'^2} \\ \rho\overline{u'v'} \\ \rho\overline{u'w'} \\ \rho\overline{v'w'} \end{bmatrix} = \begin{bmatrix} \rho\gamma \\ \rho\gamma \\ \rho\gamma \\ 0 \\ 0 \\ 0 \end{bmatrix}, \tag{12}$$

where

$$\gamma=\frac{\bar{\varepsilon}}{\bar{\lambda}},\quad \beta=\frac{\gamma}{\bar{k}},\quad \alpha=\tfrac{3}{2}\beta,\quad \lambda=\frac{1-C_{\mathrm{ASM},2}}{C_{\mathrm{ASM},1}-1+P/\bar{\varepsilon}}. \tag{13}$$

Consistent with the algebraic stress model, a higher-order approximation for the diffusion of k and ε can be obtained,[16] which replaces (8) by

$$D_\phi=\frac{\partial}{\partial x}\left\{\left[\rho C_\phi\left(\frac{\bar{k}}{\bar{\varepsilon}}\right)\overline{u'^2}+\frac{\mu}{\sigma_\phi}\right]\frac{\partial\bar{\phi}}{\partial x}+\rho C_\phi\left(\frac{\bar{k}}{\bar{\varepsilon}}\right)\overline{u'v'}\frac{\partial\bar{\phi}}{\partial r}\right\}$$
$$+\frac{1}{r}\frac{\partial}{\partial r}\left\{r\left[\rho C_\phi\left(\frac{\bar{k}}{\bar{\varepsilon}}\right)\overline{v'^2}+\frac{\mu}{\sigma_\phi}\right]\frac{\partial\bar{\phi}}{\partial r}+r\rho C_\phi\left(\frac{\bar{k}}{\bar{\varepsilon}}\right)\overline{u'v'}\frac{\partial\bar{\phi}}{\partial x}\right\}. \tag{14}$$

Note that the solution of the transport equations (7) of k and ε is still required to evaluate the algebraic stress equations (12).

Particle motion

Here it is assumed that the flow field remains unaltered by the particle movement. Thus a three-dimensional computation of particle trajectories can be performed using an independently computed two-dimensional axisymmetric flow field. Neglecting all external forces except the drag force, the equations of particle motion can be expressed in a Lagrangian reference frame as

$$\frac{\mathrm{d}u_\mathrm{p}}{\mathrm{d}t}=-\frac{u_\mathrm{p}-(\bar{u}+u')}{T_\mathrm{PR}},$$
$$\frac{\mathrm{d}v_\mathrm{p}}{\mathrm{d}t}=-\frac{v_\mathrm{p}-(\bar{v}+v')}{T_\mathrm{PR}}+\frac{w_\mathrm{p}^2}{r_\mathrm{p}}, \tag{15}$$
$$\frac{\mathrm{d}w_\mathrm{p}}{\mathrm{d}t}=-\frac{w_\mathrm{p}-(\bar{w}+w')}{T_\mathrm{PR}}-\frac{v_\mathrm{p}w_\mathrm{p}}{r_\mathrm{p}}$$

and

$$\frac{dx_p}{dt}=u_p, \qquad \frac{dr_p}{dt}=v_p, \qquad \frac{d\theta_p}{dt}=\frac{w_p}{r_p}, \tag{16}$$

where the particle relaxation time can be given as[17]

$$T_{PR}=\frac{\rho_p d_p^2}{18\mu(1+0{\cdot}15Re_p^{0{\cdot}687})}. \tag{17}$$

The fluctuational velocities (15) are modelled, using a stochastic approach,[18] as

$$u'=\eta\sqrt{(\overline{u'^2})}, \qquad v'=\eta\sqrt{(\overline{v'^2})}, \qquad w'=\eta\sqrt{(\overline{w'^2})} \tag{18}$$

where η denotes a normally distributed random variable. The RMS values of the fluctuational velocities (18) are provided by the turbulence model. Fluctuational values computed from (18) are assumed to prevail during the eddy lifetime, which is given by[18]

$$T_{EL}=\frac{C_D^{3/4}}{\sqrt{2}}\frac{\bar{k}}{\bar{\varepsilon}}. \tag{19}$$

THE FINITE ELEMENT FORMULATION AND THE SOLUTION PROCEDURE

Since the flows under consideration are highly convective, the finite element discretization equations are obtained by the streamline-upwind/Petrov–Galerkin method[6] in order to stabilize the numerical solution while introducing a minimum amount of numerical diffusion. Here a 'discontinuity-capturing' version[6] of the method is preferred to suppress the oscillations, which may occur about sharp internal layers using the streamline-upwind/Petrov–Galerkin method. Bilinear-velocity/constant-pressure elements are used in the analysis. The turbulence kinetic energy and the dissipation rate are also linearly interpolated. For the Navier–Stokes equations, 'traction-free' boundary conditions are specified at the outlet, whereas 'zero-gradient' boundary conditions are prescribed for the transport equations of k and ε.

The segregated formulation of the Navier–Stokes equations

A segregated formulation is adopted for the solution of the momentum equations (1)–(3) and the continuity equation (4). This approach is analogous to the well known finite difference procedure SIMPLE.[19] Details of the finite element formulation can be found in Reference 7. The method is based on the derivation of a discretization equation for pressure corrections p'' directly from the discretized continuity equation, considering the velocity–pressure relationships in the discretized momentum equations. This equation reads

$$\int_\Omega H_i\left\{\left[\frac{1}{a_u}\left(\frac{\partial N}{\partial x}\right)\right]_j(b_u)_{jk}+\left[\frac{1}{a_v}\left(\frac{\partial N}{\partial r}+\frac{N}{r}\right)\right]_j(b_v)_{jk}\right\}d\Omega\bar{p}_k''=-\int_\Omega H_i\left(\frac{\partial\bar{u}^*}{\partial x}+\frac{\bar{v}^*}{r}+\frac{\partial\bar{v}^*}{\partial r}\right)d\Omega. \tag{20}$$

The coefficients $(a_u)_i$ and $(a_v)_i$ in (20) denote the ith diagonal elements of the system matrices for u and v respectively. The terms $(b_u)_{ij}$ and $(b_v)_{ij}$ represent the influence coefficients of the jth pressure node to u_i and v_i respectively. The velocities u^* and v^* are the velocities based on the incorrect pressure field p^*. Corrections to the pressure field, which lead to a better satisfaction of the continuity equation, are obtained from (20). The velocities and pressures are subsequently

corrected according to

$$\bar{u}_i = \bar{u}_i^* + \frac{1}{(a_u)_i} \sum_j (b_u)_{ij} \bar{p}_j'', \tag{21}$$

$$\bar{v}_i = \bar{v}_i^* + \frac{1}{(a_v)_i} \sum_j (b_v)_{ij} \bar{p}_j'', \tag{22}$$

$$\bar{p}_i = \bar{p}_i^* + \zeta_p \bar{p}_i''. \tag{23}$$

The implementation of the algebraic stress model

For each element the Reynolds stresses are obtained by solving the system of algebraic equations (12), where the velocity gradients and other terms in the coefficient matrix (12) are evaluated at element centres. These stresses must subsequently be substituted into the Navier–Stokes equations (1)–(3) in order to be able to solve them. This coupling of the algebraically computed Reynolds stresses and the Navier–Stokes equations must be formulated carefully since it has important consequences for the numerical solution. The most straightforward way would be to write the algebraically computed Reynolds stresses on the right-hand side of the Navier–Stokes equations as prescribed source terms, while on the left-hand side only the viscous stresses remain as diffusion terms. Considering a representative stress in the axial momentum equation (1), this formulation can be expressed as follows:

$$\ldots - \frac{\partial}{\partial x}\left(2\mu \frac{\partial \bar{u}}{\partial x}\right) = \frac{\partial}{\partial x}(-\rho \overline{u'^2}) + \ldots . \tag{24}$$

Nevertheless, this straightforward formulation is computationally inconvenient. Here the numerical solution is strongly prone to divergence owing to the very small diffusion terms on the left-hand side of (24) (μ is the laminar viscosity).

In finite difference codes[20] this problem is being dealt with as follows. By manipulating the algebraic stress equations (12), a formulation is arrived at wherein the gradient of a Reynolds stress appearing in the Navier–Stokes equations is expressed by a term having a 'diffusive' structure plus additional terms. The 'diffusion-like' term is transferred to the left-hand side, whereas the additional terms remain on the right-hand side as source terms. This formulation possesses much better numerical stability compared to the previous one (equation (24)) owing to the increased diffusion on the left-hand side. However, the application of this formulation[20] using the finite element method is not straightforward. The 'diffusion-like' terms obtained for different Reynolds stresses in this formulation all have different 'diffusion coefficients'. Thus the resulting differential equations are analogous to transport equations of a medium with non-isotropic diffusion. This introduces further difficulties in applying upwind procedures. Finite element upwind procedures are all constructed for isotropic diffusion, i.e. for a scalar diffusion coefficient. In finite differences the upwind differencing can perhaps be more easily modified to take care of non-isotropic diffusion, since the orthogonal grid lines are parallel to co-ordinate directions. However, such a modification of the existing finite element upwind methods, e.g. streamline-upwinding procedures, to consider irregular meshes seems not to be very straightforward. Furthermore, this procedure[20] of coupling the Reynolds stresses with the Navier–Stokes equations produces very complicated and lengthy source terms[20], which is also an undesirable feature.

In order to avoid the above difficulties, we propose here an alternative approach for the coupling of the Reynolds stresses with the Navier–Stokes equations. In this formulation, after writing the Reynolds stresses (which are to be computed by solving the algebraic stress equations)

on the right-hand side, we add to both sides the well known turbulent viscosity approximations (equations (5) and (6)) of the Reynolds stress terms. This can be conveniently explained with the help of equation (24). For the stress term considered in equation (24) we add to both sides of the equation the term

$$-\frac{\partial}{\partial x}\left(2\mu_t \frac{\partial \bar{u}}{\partial x}-\tfrac{2}{3}\rho\bar{k}\right),$$

using the conventional definition (6) of the turbulent viscosity. This results in

$$\ldots -\frac{\partial}{\partial x}\left(2(\mu+\mu_t)\frac{\partial \bar{u}}{\partial x}-\tfrac{2}{3}\rho\bar{k}\right)=\underbrace{\frac{\partial}{\partial x}\left(-\rho\overline{u'^2}-2\mu_t \frac{\partial \bar{u}}{\partial x}+\tfrac{2}{3}\rho\bar{k}\right)}_{\text{corrective source term}}. \tag{25}$$

This procedure is applied for all stress terms in the differential equations. Thus, as can be seen from equation (25), we obtain diffusion terms on the left-hand side which are identical to the ones resulting from the conventional isotropic turbulent viscosity hypothesis (5). The non-isotropic effects are all buried in the 'corrective' source terms on the right-hand side. These 'corrective' source terms contain the differences between 'algebraic stress' (12) and 'turbulent viscosity' (5) approximations of the Reynolds stresses. In other words, in these source terms, only that portion of the algebraic Reynolds stresses are considered in which they differ from the isotropic turbulent viscosity hypothesis. Thus for flow regions where the turbulent viscosity hypothesis provides an accurate enough approximation and agrees well with the algebraic stress model, these corrective source terms vanish. For regions where the turbulent viscosity hypothesis starts to deviate from the algebraic stress model, they become 'active' and 'correct' the solution in the right direction. The implementation of the present formulation is quite easy. For a code employing the classical turbulent viscosity formulation (5), the left-hand sides of the differential equations remain completely unaltered. One only needs to add the corrective source terms (25) to the right-hand sides, which also have a relatively simple structure. Please note that we are still applying the full algebraic stress model. The formulations (24) and (25) are identical and the turbulent viscosity (6) in the present formulation (25) is only introduced for computational convenience. The transport equations of k and ε are also coupled with the algebraic Reynolds stresses using the corrective source term approach. No special difficulties are encountered in the computations performed using the present formulation. The convergence rate is also observed to be similar to that of the k–ε model.

The near-wall treatment

Owing to the difficulties associated with the modelling of turbulent flow near solid boundaries, a wall-functions approach[8] is adopted. Here it is assumed that the following equations hold within the wall layer:

$$u^+ = \begin{cases} y^+ & \text{for } y^+ < 11{\cdot}6, \\ (1/\kappa)\ln(Ey^+) & \text{for } y^+ \geqslant 11{\cdot}6, \end{cases} \tag{26}$$

$$\bar{k}=u_\tau^2/C_D^{1/2}, \tag{27}$$

$$\bar{\varepsilon}=C_D^{3/4}k^{3/2}/\kappa y. \tag{28}$$

Thus boundary nodes can be placed not at the wall but at a distance from the wall, the boundary conditions being derived from (26)–(28). To evaluate (26)–(28), the wall shear stress must be known.

The present approach for the estimation of the wall shear stress was discussed in Reference 9. A possible extension of the recursive shear stress formulae[9] for a wall element with irregular shape (Figure 1) is given below:

$$\tau_w = \begin{cases} \dfrac{\mu \bar{U}_{p2}}{y_2} & \text{for } y_2^+ < 11{\cdot}6, \\ \dfrac{\kappa C_D^{1/4} \rho \bar{U}_{p2} \bar{k}_1^{1/2}}{\ln(E C_D^{1/4} \rho y_2 \bar{k}_1^{1/2}/\mu)} & \text{for } y_2^+ \geqslant 11{\cdot}6. \end{cases} \tag{29}$$

In (29), U_p denotes the wall-parallel component of the velocity vector. For inclined walls, U_p must also replace u in (26).

The computation of particle trajectories

Assuming sufficiently small time increments, in which the gas velocities and body force terms remain constant,[18] equations (15) can be integrated analytically to give

$$\begin{aligned} u_p &= \bar{u} + u' + (u_{p0} - \bar{u} - u') \exp(-\Delta t/T_{PR}), \\ v_p &= \bar{v} + v' + T_{PR} w_p^2/r_{p0} + (v_{p0} - \bar{v} - v' - T_{PR} w_p^2/r_{p0}) \exp(-\Delta t/T_{PR}), \\ w_p &= \bar{w} + w' - T_{PR} v_{p0} w_{p0}/r_{p0} + (w_{p0} - \bar{w} - w' + T_{PR} v_{p0} w_{p0}/r_{p0}) \exp(-\Delta t/T_{PR}), \end{aligned} \tag{30}$$

where the subscript 0 denotes the conditions at beginning of the time increment. Instantaneous particle co-ordinates are obtained by a stepwise integration of equations (16).

The solution procedure

The important steps of the solution procedure can be summarized as follows.

1. Guess initial fields for u, v, w, p, k, ε and μ_t.

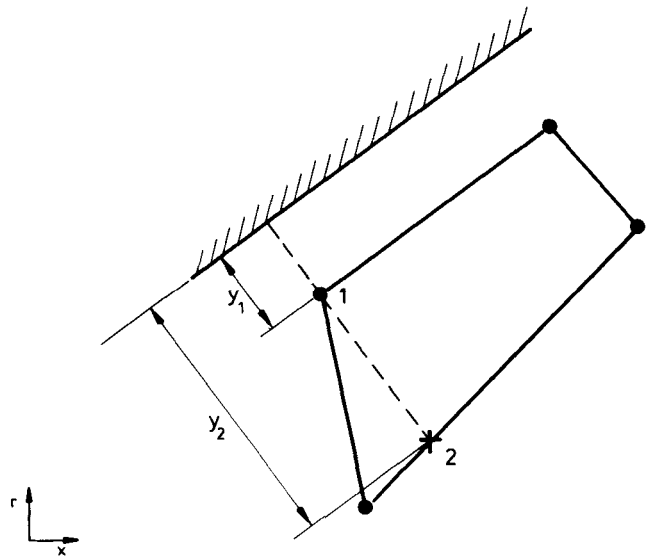

Figure 1. An element near the wall

2. Compute Reynolds stresses from algebraic stress equations (12).
3. Solve (1) for u.
4. Solve (2) for v.
5. Solve (20) for p'' and compute the new pressure field from (23).
6. Correct the velocity field according to (21), (22).
7. Solve (3) for w.
8. Solve (7) for k.
9. Solve (7) for ε.
10. Update μ_t and wall boundary conditions ((6), (26)–(29)).
11. Go to step 2 if convergence is not achieved.
12. If required, compute particle trajectories ((15)–(19), (30)) using the converged solution of the flow field.

The solution of the finite element discretization equations for each field variable is obtained by a direct solver using a band matrix storage mode. Underrelaxation is employed for u, v, w, k and ε. μ_t is also underrelaxed. The standard k–ε model can be recovered by omitting step 2 of the above procedure and setting the corrective source terms (25) equal to zero.

RESULTS

As a numerical example, a test case[21] of the International Flame Research Foundation (IFRF) is considered. Measurements were performed by an LDA technique. The flow geometry and the finite element mesh are shown in Figures 2 and 3 respectively.

The swirl generator produces a simple solid body rotation with a nearly uniform axial velocity profile. The mean axial velocity and the swirl number at the inlet are 4·7 m s^{-1} and 0·7 respectively. For computations the measured profiles of the axial and tangential velocity are prescribed as inlet boundary conditions. The radial velocity is specified as zero at the inlet. The values of the turbulent kinetic energy are derived from the measured $\overline{u'^2}$ and $\overline{w'^2}$ profiles, assuming locally at the inlet that

$$\overline{v'^2} = (\overline{u'^2} + \overline{w'^2})/2{\cdot}0. \tag{31}$$

The inlet conditions for the turbulence dissipation rate are obtained from

$$\bar{\varepsilon} = C_D^{3/4} \bar{k}^{3/2}/0{\cdot}01R. \tag{32}$$

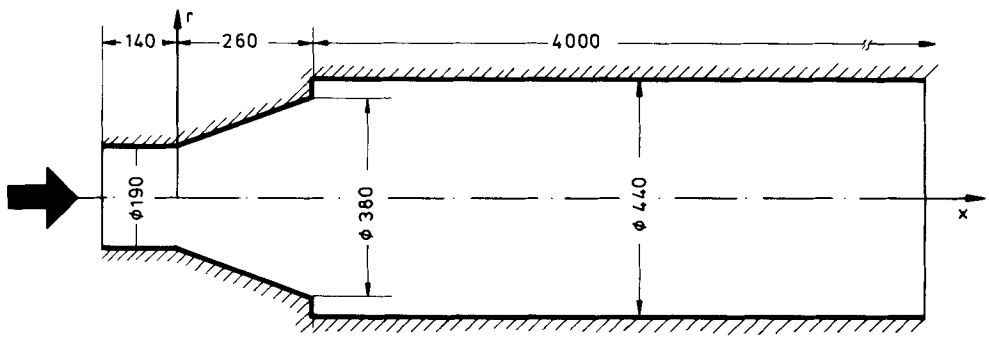

Figure 2. The geometry (dimensions in millimetres)

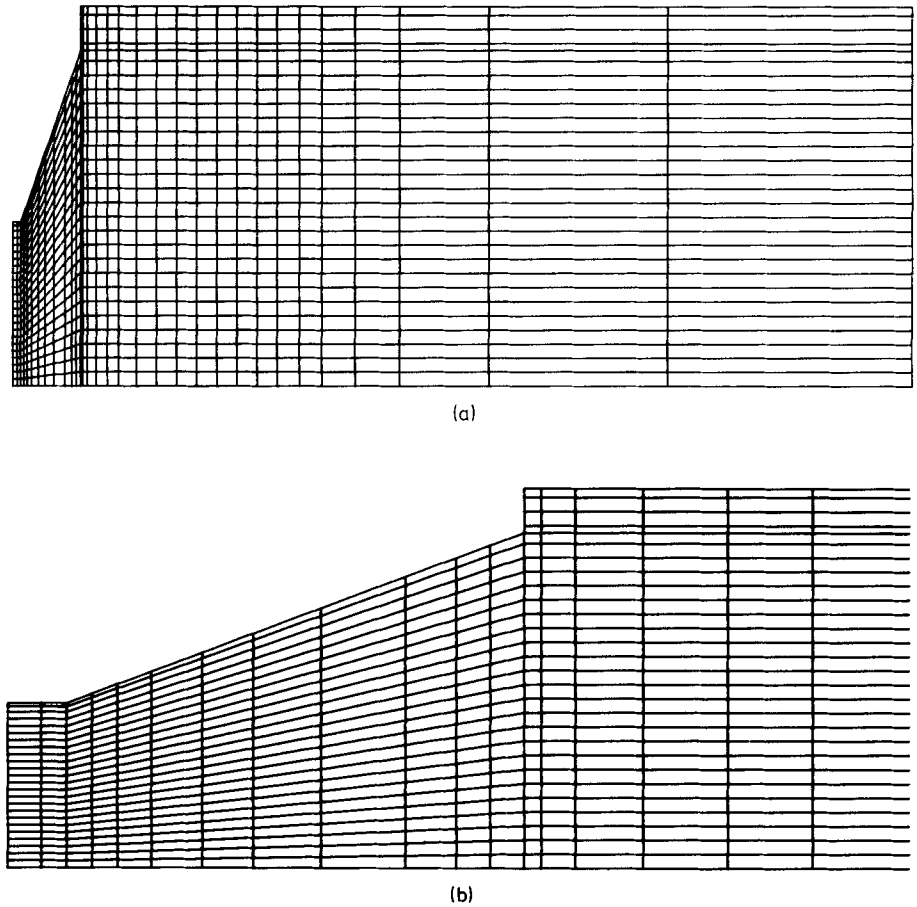

Figure 3. The finite element mesh: (a) whole domain; (b) inlet region (same plotting scale in the x- and r-directions)

The following set of constants are employed in the present study:[20]

$$C_D = 0{\cdot}09,\ C_1 = 1{\cdot}43,\ C_2 = 1{\cdot}92,\ \sigma_{k,e} = 1{\cdot}0,\ \sigma_{\varepsilon,e} = 1{\cdot}3,\ C_k = 0{\cdot}22,$$
$$C_\varepsilon = 0{\cdot}15,\ C_{\mathrm{ASM},1} = 2{\cdot}5,\ C_{\mathrm{ASM},2} = 0{\cdot}55.$$

k–ε model results

In this subsection the results obtained using the k–ε model are presented. Vector plots of the velocity field (u- and v-velocities) are presented in Figure 4 for the non-swirling and swirling flows. Without swirl the flow separates near the inlet as it expands within the quarl and an external recirculation zone is formed. With swirl the velocities near the walls of the quarl become very high and the external recirculation zone disappears; instead, an internal recirculation zone is created. Radial profiles of axial and tangential velocities at several axial locations are presented in Figures 5 and 6 respectively; the results are compared with experiment[21] and finite difference predictions.[22] The finite difference results[22] were obtained using a 27 × 23 grid, the k–ε model and hybrid differencing. This grid is coarser than the present finite element one (32 × 28) (Figure 2), but a

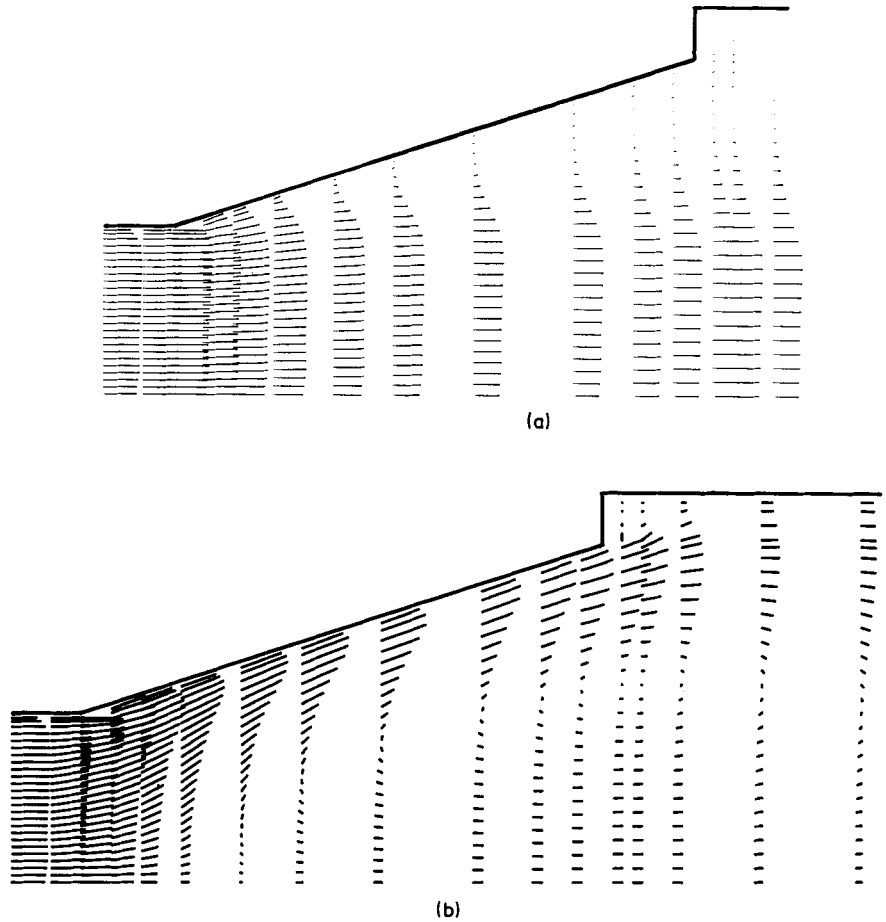

Figure 4. Velocity fields (k–ε model): (a) without swirl; (b) with swirl (swirl number at inlet is 0·7)

refinement of the finite difference grid up to 30×30 was reported[4] to bring no remarkable improvement. Inspection of the experimental results (Figure 5) shows that the axial velocity has positive values about the centreline for the first three axial locations, i.e. the central part of the jet penetrates through the recirculation zone. This behaviour is not predicted by either method. However, comparison of the finite element and finite difference results for axial (Figure 5) and tangential (Figure 6) velocities shows that the finite element results agree everywhere better with experiment. This can at least partly be attributed to the different amounts of false diffusion produced in the two models. The finite element results are apparently subject to less amounts of false diffusion, owing to the streamline upwinding (which is less diffusive than the hybrid differencing) and the alignment of the grid lines with the flow direction (more or less) within the quarl (Figures 2–4). A further aspect is the discretization of the inclined quarl wall (Figures 2 and 3). By finite elements the inclined wall of the quarl can be perfectly discretized (Figure 3). In the finite difference model[22] the quarl wall was approximated as a 'staircase', which means a further source of error, as also indicated by discrepancies between finite difference predictions and experiment especially in the near-wall regions.

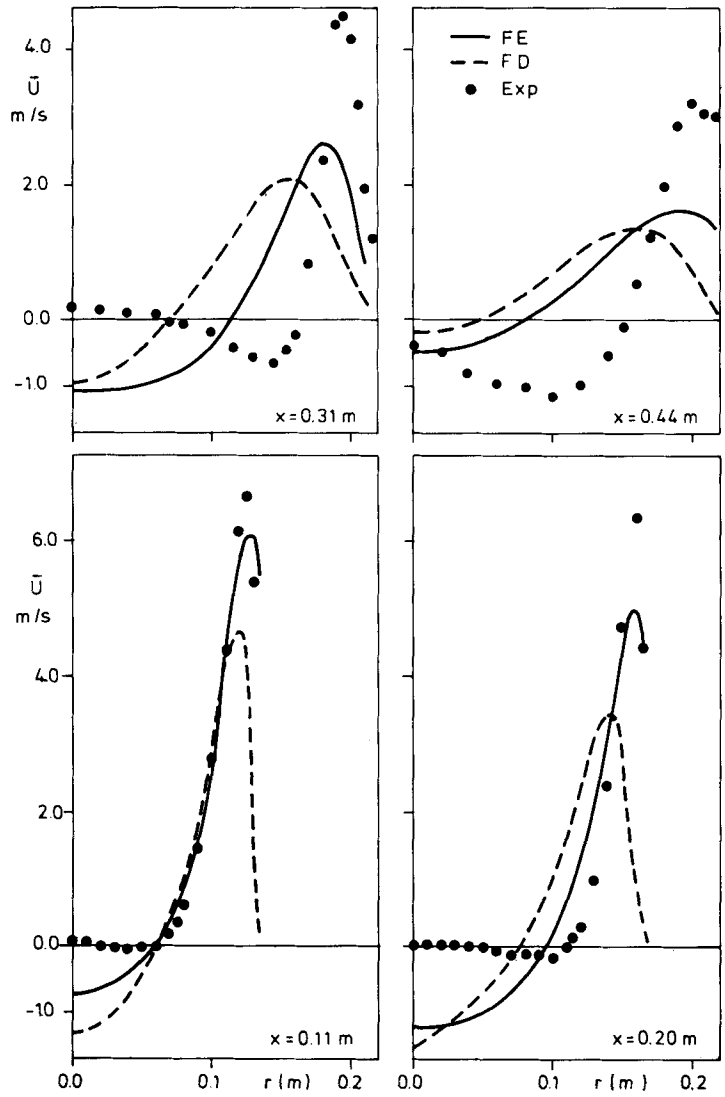

Figure 5. Radial profiles of the axial velocity (k–ε model)

A comparison of upwind procedures

Here the results are also obtained using the quadrature-upwind scheme[23] (QU), which is known to be more diffusive than the 'discontinuity-capturing' streamline-upwind/Petrov–Galerkin method[6] (SUPGDC). In Figure 7, radial profiles of axial and tangential velocities are compared. The QU curves are clearly 'smeared' compared to the SUPGDC ones. This comparison confirms that the level of false diffusion introduced by the upwind scheme can substantially affect the results in such flow situations.

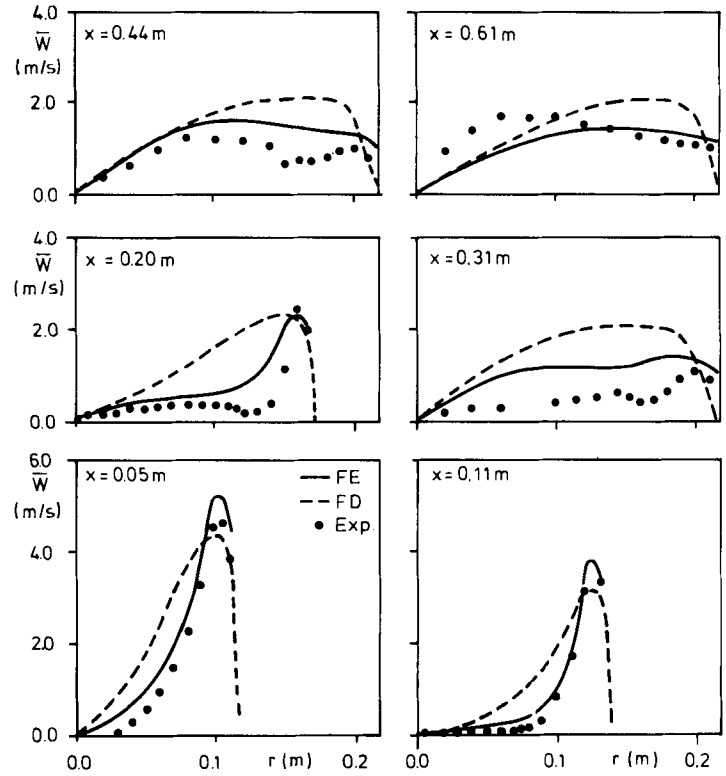

Figure 6. Radial profiles of the tangential velocity (k–ε model)

Algebraic stress model (ASM) results

In this subsection the results obtained by the algebraic stress model (12), (25) are presented. Figure 8 illustrates the computed velocity field. A comparison with Figure 4 shows that the inner recirculation zone predicted by the algebraic stress model is larger compared to the k–ε model results, where the 'eye' of the recirculation zone has moved further downstream and the negative velocities near the centreline have become smaller. In Figure 9, radial profiles of the axial velocity obtained by the algebraic stress model are compared with the k–ε results and experiments. The algebraic stress model shows a much better agreement with experiment, where the centreline values, the gradients about the edges of the forward flow region and the peaks of the velocity profiles are all more accurately predicted.

Radial profiles of the tangential velocity are presented in Figure 10. The algebraic stress model shows also here a clearly better agreement than the k–ε model with experiment.

The boundaries of the internal recirculation zone predicted by the algebraic stress and the k–ε models are compared with experiment in Figure 11. The forward flow region within the internal recirculation zone could not be predicted by either method. However, the algebraic stress model gives a much better prediction of the outer envelope of the internal recirculation zone.

A code using the k–ε model must be modified at three places (apart from writing an additional subroutine for the computation of the algebraic Reynolds stresses (12)) in order to apply the

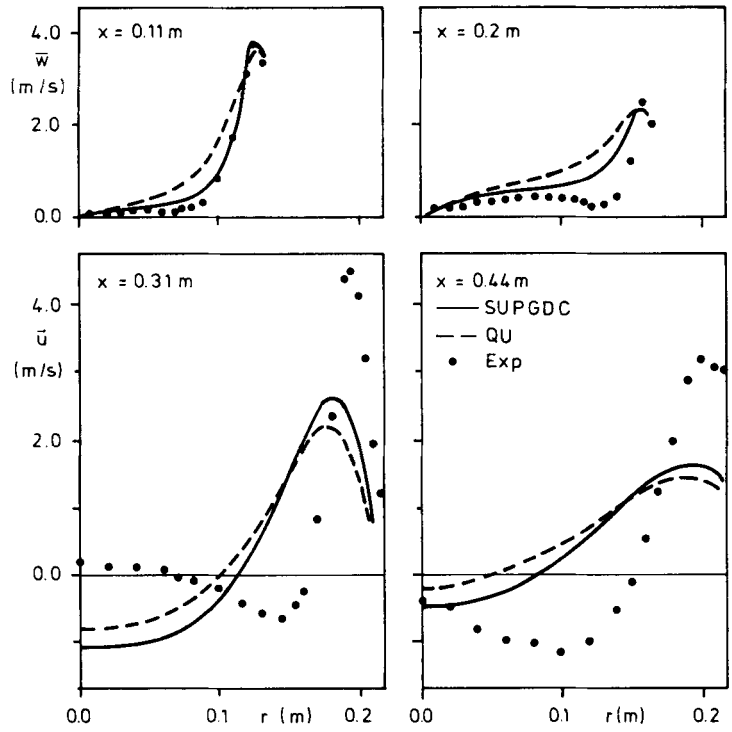

Figure 7. Comparison of the streamline and quadrature upwinding (k–ε model)

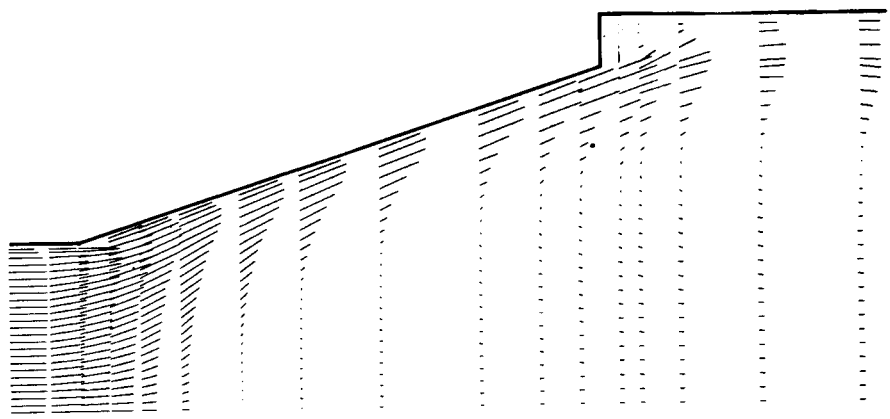

Figure 8. The velocity field (ASM)

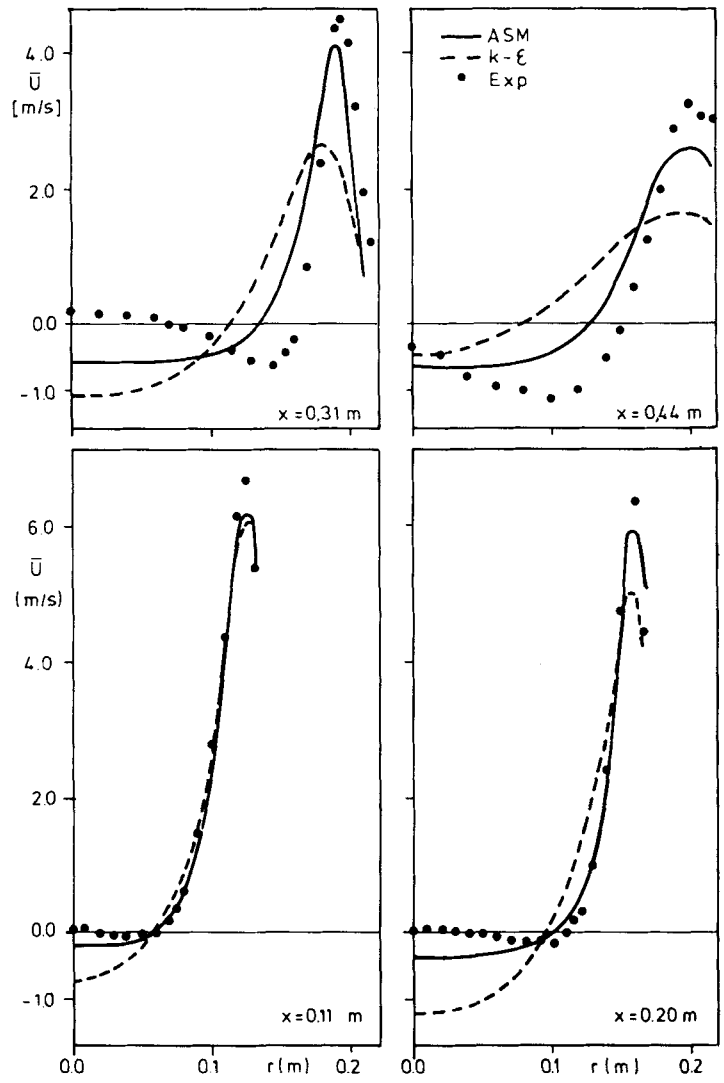

Figure 9. Radial profiles of the axial velocity

algebraic stress model. Here we performed a numerical experiment, where these modifications are introduced stepwise in separate runs, in order to see the effect of different levels of applying the algebraic stress model. In the first run (ASM1) only the Navier–Stokes equations are modified by replacing the turbulent viscosity approximations (5) by the algebraic stresses (12) (using the corrective source term approach (25)). In the second run (ASM2), in addition to the first modification, the production term of k, (11), is modified by substituting the algebraic Reynolds stresses (12) instead of the turbulent viscosity approximations (5) into the expression (11). In the third run (ASM3), which represents the 'full' application of the algebraic stress model, the diffusion terms of the transport equations of k and ε are also computed consistent with the algebraic stress model replacing (8) by (14) (here also the corrective source term approach (25) is used).

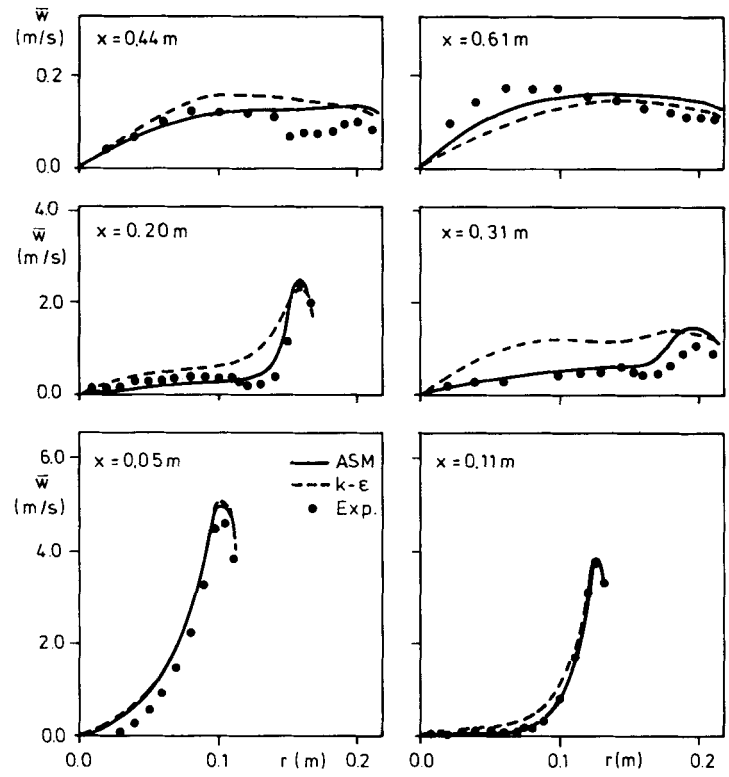

Figure 10. Radial profiles of the tangential velocity

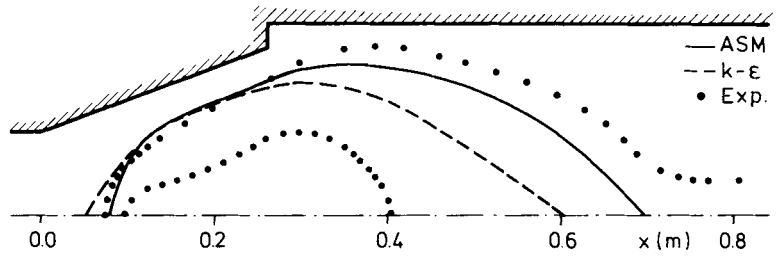

Figure 11. Boundaries of the internal recirculation zone

Results are compared in Figure 12. Here profiles of axial and tangential velocity at only one axial location are considered, but the tendencies are similar everywhere. It can be seen from the figure that the largest deviation from the k–ε model is obtained by only modifying the Navier–Stokes equations (ASM1). The modification of the production term of the turbulent kinetic energy (ASM2) introduces a further improvement which is quantitatively smaller. The ASM2 and ASM3 curves are almost identical, implying that the additional modification of the diffusion terms of turbulence quantities practically does not affect the results.

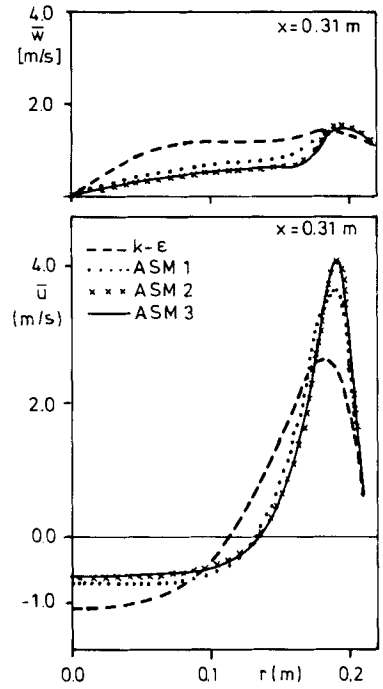

Figure 12. Comparison of different levels of applying the ASM

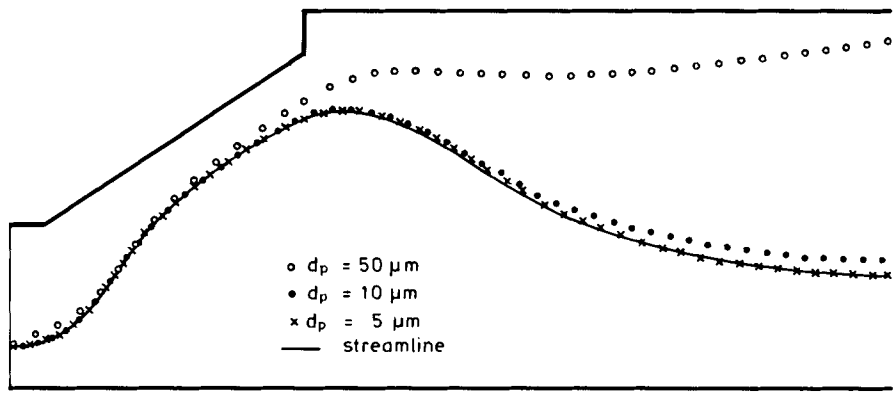

Figure 13. Particle paths for three size classes (neglecting turbulence)

Particle trajectories

The computation of particle trajectories is based upon the converged flow field solution. The particle velocities at the injection point are assumed to be identical with the local fluid velocities. First the influence of particle size is investigated. Here the influence of turbulence is neglected by setting the fluctuational values of the velocities in (15) and (30) equal to zero. Three sizes are considered: $d_p = 50$, 10 and 5 μm. The size $d_p = 50$ μm corresponds to the mean particle size

in pulverized coal combustion. Particle densities are also set to a representative value for coal. The particles are injected at the inlet at $r=R/4$, and $\theta=0$. The projections of the particle paths on the $\theta=0$ plane and the streamline originating from the particle injection point are plotted in Figure 13. The results show that only very small particles ($d_p=5$ μm) are able to follow the fluid motion, whereas the trajectories deviate strongly from the streamline with increasing particle size.

Turbulence effects are considered by computing the fluctuational velocities according to (18). Particle trajectories with turbulence effects (random walk) are presented in Figure 14 for two particles.

A comparison of Figures 13 and 14 demonstrates that the particle paths computed with turbulence effects may differ considerably from those obtained neglecting the turbulence. In the lower illustration in Figure 14 the particle falls into the recirculation zone (Figures 8 and 11) because of the turbulent movements (instead of sliding smoothly along the separating streamline as predicted by neglecting the turbulence (Figure 13)) and makes many turns within the recirculation zone before it can escape from the rear part, which results in an approximately 10 times larger residence time compared to the case neglecting turbulence.

To investigate the effect of turbulence modelling on the prediction of turbulent particle dispersion, particle trajectories are computed using both the k–ε model and the algebraic stress

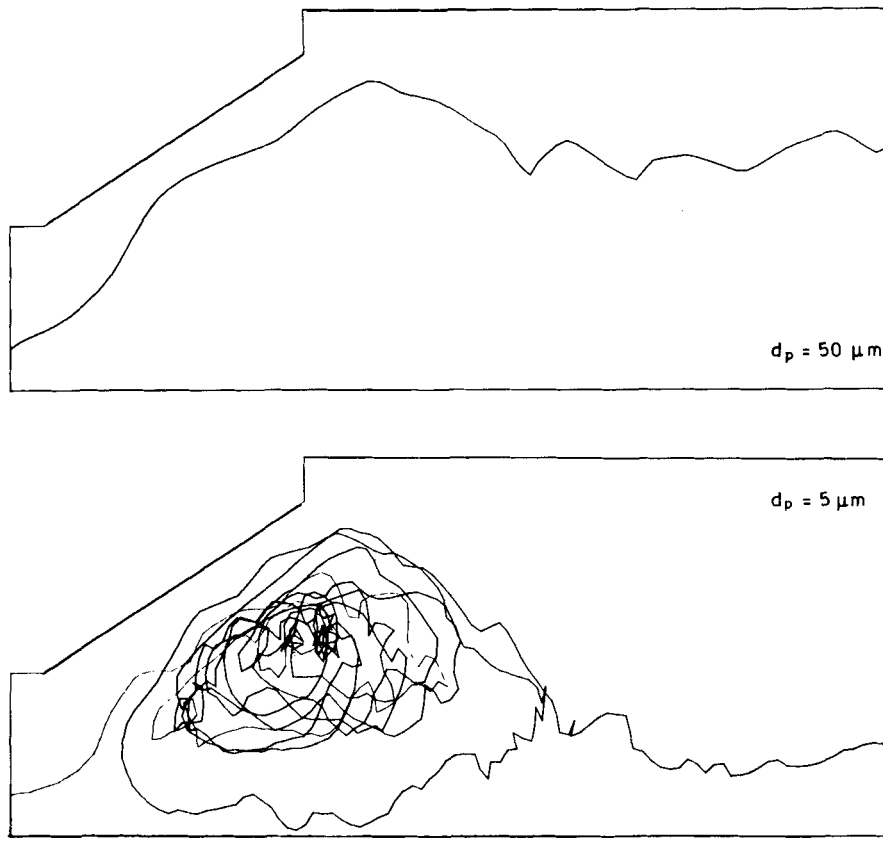

Figure 14. Particle paths with turbulence effects (random walk)

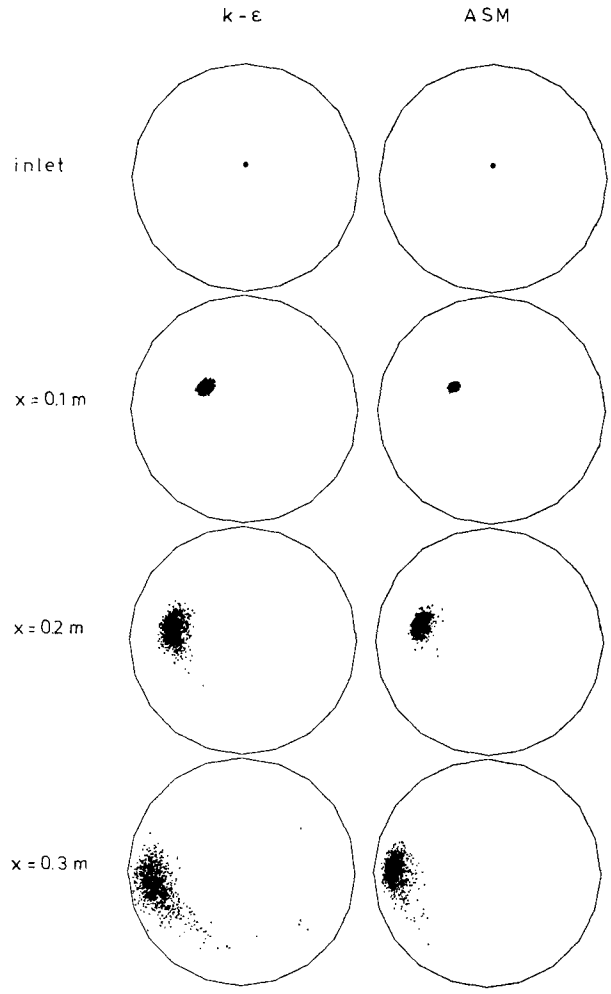

Figure 15. Pierce points of particles through several cross-sections

model for 1000 particles injected at the same location. In Figure 15 the 'pierce points' of these particles through several cross-sections are plotted. The figure shows how the particle cloud rotates owing to the swirling gas motion and at the same time is dispersed by turbulent movements as it proceeds in the axial direction. Inspecting the figure, one can observe that the k–ε model overestimates the turbulent particle dispersion in comparison to the algebraic stress model.

CONCLUSIONS

The application of the finite element method to confined turbulent swirling flow problems has been investigated. The analysis has been extended to predict particle motion in turbulent swirling flow fields. A convenient way of implementing the algebraic stress model in finite elements has been proposed. It has been shown that improved results can be obtained using less diffusive upwind schemes and the algebraic stress model instead of the k–ε model. Nevertheless, some

features of the flow field (forward flow region within the internal recirculation zone) could still not be predicted satisfactorily. However, the prediction quality is expected to improve by employing the Reynolds stress transport model, which will be investigated in a future work.

ACKNOWLEDGEMENTS

This work was carried out within the TECFLAM Project on Mathematical Modelling and Laser Diagnostics of Technical Flames. Funding by the German Ministry of Research and Technology (BMFT) and the Federal Government of Baden-Württemberg is gratefully acknowledged.

APPENDIX: NOMENCLATURE

$C_D, C_1, C_2, C_\phi, C_{ASM,1}, C_{ASM,2}$	constants in turbulence models
d_p	particle diameter
E	constant in turbulence wall model
H_i	pressure shape functions
k	turbulence kinetic energy
N_i	velocity shape functions
p	pressure
r	radial co-ordinate
R	pipe radius at the inlet
Re_p	particle Reynolds number
t	time
T_{EL}	eddy lifetime
T_{PR}	particle relaxation time
u	axial velocity
U_p	velocity component parallel to wall
u_τ	shear velocity
v	radial velocity
w	tangential velocity
x	axial co-ordinate
y	distance from the wall

Greek symbols

Δ	incremental change
ε	dissipation rate of k
ζ_p	underrelaxation factor for pressure
θ	azimuthal co-ordinate
κ	von Karman's constant
μ	molecular viscosity
μ_t	turbulent viscosity
ρ	density
σ	Prandtl number
τ_w	wall shear stress
ϕ	a field variable

Subscripts

e	effective
0	conditions at the beginning of a time step
p	particle
t	turbulent
w	wall

Superscripts

$(\bar{})$	Reynolds-averaged value
$()'$	fluctuational value
$()''$	correction value
$()^*$	uncorrected value
$()^+$	quantity non-dimensionalized by means of μ, τ_w and ρ

REFERENCES

1. A. K. Gupta, D. G. Lilley and N. Syred, *Swirl Flows*, Abacus Press, Kent, 1984.
2. A. C. Benim, 'Finite element solution of an enclosed diffusion flame', *Int. j. numer. methods fluids*, **9**, 289–303 (1989).
3. A. C. Benim, W. Zinser and U. Schnell, 'Investigation into the finite element analysis of enclosed turbulent diffusion flames', *Appl. Math. Modell.*, **13**, 258–267 (1989).
4. U. Schnell, K. Görner and A. C. Benim, 'Mathematische Modellierung von Kohlenstaubflammen—Methoden und Teilmodelle', *Proc. 3rd TECFLAM Seminar*, Karlsruhe, ISBN 3-926751-05-3, 1987, pp. 149–164.
5. J. G. Rice and R. J. Schnipke, 'A monotone streamline upwind finite element method for convection-dominated flows', *Comput. Methods Appl. Mech. Eng.*, **48**, 313–327 (1985).
6. T. J. R. Hughes, M. Mallet and A. Mikuzami, 'A new finite element formulation for computational fluid dynamics: II. Beyond SUPG', *Comput. Methods Appl. Mech. Eng.*, **54**, 341–355 (1986).
7. A. C. Benim and W. Zinser, 'A segregated formulation of Navier–Stokes equations with finite elements', *Comput. Methods Appl. Mech. Eng.*, **57**, 223–237 (1986).
8. B. E. Launder and D. B. Spalding, *Mathematical Models of Turbulence*, Academic Press, London, 1972.
9. A. C. Benim and W. Zinser, 'Investigation into the finite element analysis of confined turbulent flows using a k–ε model of turbulence', *Comput. Methods Appl. Mech. Eng.*, **51**, 507–523 (1985).
10. A. G. Hutton, R. M. Smith and S. Hickmott, 'The computation of turbulent flows of industrial complexity by the finite element method—progress and prospects', *Int. j. numer. methods fluids*, **7**, 1277–1297 (1987).
11. J. L. Sohn, 'Evaluation of FIDAP on some classical laminar and turbulent benchmarks', *Int. j. numer. methods fluids*, **8**, 1469–1490 (1988).
12. K. Y. Kim and M. K. Chung, 'New eddy viscosity model for computation of swirling turbulent flows', *AIAA J.*, **25**, 1020–1022 (1987).
13. M. A. Leschziner and W. Rodi, 'Computation of strongly swirling axisymmetric free jets', *AIAA J.*, **22**, 1742–1747 (1984).
14. L. Krishnamurthy and S. O. Park, 'Streamline curvature effects in confined recirculating flowfields behind an axisymmetrical bluff body: numerical calculations with the k–ε turbulence model', *Proc. 4th Symp. on Turbulent Shear Flows*, Karlsruhe, 1983, pp. 19.1–19.6.
15. W. Rodi, 'A new algebraic relation for calculating the Reynolds stresses', *ZAMM*, **56**, 219–221 (1976).
16. B. E. Launder and A. Morse, 'Numerical predictions of axisymmetric free shear flows with a Reynolds stress closure', in F. Durst, B. E. Launder, F. W. Schmidt and J. H. Whitelaw (eds.), *Turbulent Shear Flows I*, Springer, Berlin, 1979, pp. 279–294.
17. F. Durst, D. Milojevic and B. Schönung, 'Eulerian and Lagrangian predictions of particulate two-phase flows: a numerical study', *Appl. Math. Modell.*, **8**, 101–115 (1984).
18. F. Boysan, W. H. Ayers and J. Swithenbank, 'A fundamental mathematical modeling approach to cyclone design', *Trans. IChemE*, **60**, 222–230 (1982).
19. S. V. Patankar, *Numerical Heat Transfer and Fluid Flow*, McGraw-Hill, New York, 1980.
20. D. S. Sloan, P. J. Smith and L. D. Smoot, 'Modeling of swirl in turbulent flow systems', *Prog. Energy. Combust. Sci.*, **12**, 163–250 (1986).
21. A. Hagiwara, S. Borz and R. Weber, 'Theoretical and experimental studies on isothermal expanding swirling flows with application to swirl burner design—results of the NFA 2-1 investigations', *IFRF Report., Doc. F 259/a/3*, 1986.
22. A. Wanik and U. Schnell, 'Some remarks on the Piso and Simple algorithms for steady turbulent flow problems', *Comput. Fluids*, **17**, 555–570 (1989).
23. T. J. R. Hughes, 'A simple scheme for developing "upwind" finite elements', *Int. j. numer. methods eng.*, **12**, 1359–1365 (1978).